science.sciencemag.org/content/367/6479/773/suppl/DC1

Supplementary Materials for

Ionoelastomer junctions between polymer networks of fixed anions and cations

Hyeong Jun Kim, Baohong Chen, Zhigang Suo*, Ryan C. Hayward*

*Corresponding author. Email: hayward@umass.edu (R.C.H.); suo@seas.harvard.edu (Z.S.)

Published 14 February 2020, *Science* **367**, 773 (2020)
DOI: 10.1126/science.aay8467

This PDF file includes:

Materials and Methods
Supplementary Text
Figs. S1 to S21
Tables S1 to S4
References

Materials and Methods

1. General

Unless otherwise noted, commercially available reagents were used without further purification. Thermal initiator 2,2'-azobisisobutyronitrile (AIBN, Sigma-Aldrich, 441090-25G) was recrystallized from methanol before use. Poly(ethylene glycol) diacrylate (PEGDA, average M_n 250, Sigma-Aldrich, 475629-100ML) was purified by passing through an activated basic aluminum oxide (Sigma-Aldrich) short column. Glass substrates were fluorinated using silane chemistry as follows. Microscope slides (Fisher Scientific, 1 mm thickness) were cleaned thoroughly with ultrasonication in acetone, DI water, and isopropanol. Each side of the glass slide was subjected to UV-Ozone treatment for 15 min followed by exposing to tridecafluoro-1,1,2,2-tetrahydrooctyl dimethyl chlorosilane (Gelest, SIT8170.0) vapor at 100°C overnight. Next, fluorinated glass slides were thoroughly washed with ethanol and dried at 60°C in an oven.

2. 1-ethyl-3-methyl imidazolium (3-sulfopropyl) acrylate (ES)

ES was synthesized following the previous work (**Fig. S1A**) (*23*). We mixed 6.3 g (43.0 mmol) of 1-ethyl-3-methylimidazolium chloride ([EMIM]Cl, Iolitec Inc., IL-0093-HP) and 10.0 g (43.0 mmol) of 3-sulfopropyl acrylate potassium salt (K[SPA], Sigma-Aldrich, 251631-100G) in 30 mL of acetonitrile. In the presence of 10 mg of methoxyphenol (Sigma-Aldrich, 54050-100G) as an inhibitor, the mixture was vigorously stirred overnight at room temperature. The precipitated potassium chloride (KCl) was filtered and solvent was removed via a rotary evaporator. A crude solution was dried under 10^{-1} torr for complete evaporation of acetonitrile. A residual liquid was re-dissolved in fresh dichloromethane (DCM) and the solution was kept at < 0 °C overnight. Precipitated salts were filtrated. After complete removal of DCM, a viscous yellow oil product was obtained (6.8 g, yield 52%). Purity > 98 % as calculated by ^{1}H-NMR (**Fig. S1B**, 500 MHz, D_2O): 8.61 (s, 1H, H2 (imidazole)), 7.39 (s, 1H, H4 (imidazole)), 7.32 (s, 1H, H5(imidazole)), 6.37-5.88 (m, 3H, CH_2=CH-), 4.21 (t, 2H, CO-O-CH_2-), 4.15-4.11 (m, 2H, N-CH_2-), 3.79 (s, 3H, N-CH_3), 2.94 (t, 2H, -CH_2-S), 2.08-2.03 (m, 2H, CO-O-CH_2-CH_2-), 1.40 (t, 3H, N-CH_2-CH_3).

3. 1–[2–acryloyloxyethyl]–3–buthylimidazolium bis(trifluoromethane) sulfonimides (AT)

The synthetic scheme for AT is shown in **Fig. S2A**. Under N_2 atmosphere, 5.0 g (27.9 mmol) of 2-bromoethyl acrylate (stabilized with 900-1500 ppm of 4-methoxyphenol, Alfa Aesar, L12502-06) and 3.64 g (29.31 mmol, 1.05 eq) of 1-butylimidazole (Sigma-Aldrich, 348414-100G) was mixed in 30 mL of fresh acetonitrile and stirred overnight at 60 °C. After reaction, acetonitrile was removed via a rotary evaporator. 1–[2–acryloyloxyethyl]–3–buthylimidazolium bromide ([AEBI]Br) was extracted by DI water followed by washing with DCM at least three times. Then, 8.0 g (27.9 mmol, 1 eq) bis(trifluoromethane)sulfonimide lithium (Li[TFSI]) salt (Sigma-Aldrich, 544094-25G) was added to the aqueous solution of [AEBI]Br and stirred overnight at room temperature. After ion-exchange, water immiscible AT was extracted with DCM and washed with DI water at least three times. Residual water in the organic layer was then dried over $MgSO_4$. Drying of final product AT under vacuum < 10^{-1} torr resulted in a slightly yellow transparent liquid (5.7 g, yield 41%). The monomer so obtained contains < 10 mol % of 1-butylimidazole as an impurity, which is removed in a subsequent step by DCM extraction after polymerization of AT. ^{1}H-NMR (**Fig. S2B**, 500 MHz, D_6-DMSO): 9.23 (s, 1H, H2 (imidazole)), 7.81 (d, 2H, H4 H5 (imidazole)), 6.35-5.99 (m, 3H, CH_2=CH-), 4.51-4.49 (m, 4H, CO-O-CH_2-CH_2), 4.19 (t, 2H, N-

CH_2-), 1.79-1.73 (m, 2H, N-CH_2-CH_2), 1.25-1.20 (m, 2H, N-CH_2-CH_2-CH_2-), 0.89 (t, 3H, -CH_3). ^{19}F-NMR (**Fig. S2C**, 500 MHz, D_6-DMSO): δ =79.9 (s, 6F, -CF_3).

4. Preparation of carbon nanotube/glass substrate

Carboxylic acid functionalized (> 8%) multi-walled carbon nanotubes (Sigma-Aldrich, 755125-1G) were dispersed in dimethylformamide (2 mg/mL). The solution was subjected to horn sonication (Qsonica) for 1 h. Undispersed carbon nanotubes were separated from the solution by centrifugation for 10 min at 5000 rpm. A glass substrate with the dimension of 2.5 cm × 4 cm was held at 150 ^{o}C on a hotplate, and the carbon nanotube solution was sprayed using a commercial air-brush (Iwata Eclipse HP-CS) at a distance of ~ 15 cm and pressure of ~ 25 psi following the previous work (*32*). The weight increases of substrates after coating with various amounts of carbon nanotube solution were measured (**Table S1**). Four-point probe method (The Pro4) was used to measure corresponding sheet resistance. For ionoelastomer devices, we used 5 mL of carbon nanotube solution for spray coating, resulting in a weight increase by 0.7 ± 0.3 mg and sheet resistance of 549 ± 27 Ω/sq. An SEM image (Magellan 400) of the deposited carbon nanotube film is shown in **Fig. S3A** and the distribution of sheet resistance in the film is shown **Fig. S3B**.

5. Preparation of ionoelastomer devices

A schematic illustration of the preparation of ionoelastomer junction is shown in **Fig. S4**. We vigorously mixed 0.2 g of ES (or AT) with 2 mol% purified PEGDA. Next, 0.5 mol% of AIBN solution in ethanol (10 mg/mL) was added. After mixing, ethanol was removed under vacuum of $< 10^{-1}$ torr at room temperature. The viscous mixture was then injected into a glass mold of carbon nanotube/glass and fluorinated-glass separated by 250 μm thick poly(tetrafluoroethylene) (PTFE) spacers. Free radical polymerization was initiated at 60 ^{o}C under N_2. After reacting overnight, unreacted monomers were extracted by washing with DCM. The extracted fraction was measured to be ~ 2 wt% for ES and ~ 10 wt% for AT. Finally, ionoelastomers were dried at 60 ^{o}C in a vacuum oven to remove residual solvents and water before use.

We note that the AT ionoelastomer is hydrophobic due to the use of a fluorinated TFSI anion, and incorporation of a small amount of PEGDA (2 mol%) does not induce measurable absorption of water (**Fig.S6, S8**). However, ES ionoelastomer is hygroscopic; it can absorb up to ~30 wt% of water in ambient conditions. Therefore, we stored ES in a desiccator with drying agent and heated to 60 ^{o}C under vacuum for 3 h prior to use. After drying, a small amount of residual water (< 2 wt%) was observed in ES, as evidenced by thermogravimetric analysis (TGA) (**Fig. S6B**) and attenuated total reflectance Fourier transform infrared spectroscopy (ATR-FTIR) (**Fig. S6C**). Ionic conductivity changes of ionoelastomers stored in ambient condition (23 ^{o}C and 33 % RH) over time are shown in Fig. S6D. Hydrophobic AT shows almost no change in ionic conductivity for 96 h. However, ES absorbs water molecules and its conductivity increase by a factor of 4 (to 2.4×10^{-3} mS/cm) compared to the initial value (5.7×10^{-4} mS/cm) after 96 h of exposure.

We observed that the carbon nanotube layers were successfully transferred from the glass substrate and embedded on one side of the resulting ionoelastomers. SEM images of the carbon nanotube embedded side of the ES and AT are shown in **Fig. S3C, S3D**, respectively. After drying, free standing ionoelastomers of ES or AT (1 cm × 1 cm × 250 μm) were carefully peeled off of the substrate, and bilayer junctions of ES/ES, AT/AT and ES/AT were then prepared by simply attaching the two bare surfaces of the ionoelastomers. For ionoelastomer transistors, two ES (0.5 cm × 1 cm × 250 μm) layers separated by a lateral gap of < 1 mm were attached on an AT film (1 cm × 1 cm × 250 μm). Finally, all devices were encapsulated between two layers of VHB 4905 adhesive (3M) to electrically insulate the ionoelastomer junction devices.

6. Preparation of ES/AT ionoelastomer devices with microporous carbon electrode

Microporous layer (MPL) carbon electrodes (39BC, Sigracet; **Fig. S12A**) were applied to increase the capacitance asymmetry between EDL and IDL. ES (or AT) monomer was mixed with 2 mol% PEGDA and 0.5 mol% AIBN. Then, 0.1 g of this solution was diluted with 500 μL of ethanol and drop-casted onto a 2.5 cm × 4 cm piece of MPL electrode. The ethanol was allowed to evaporate for 12 h at room temperature followed by polymerization under N_2 condition in a 60 ^{o}C oven for overnight. After this first polymerization step, the coated MPL electrode was placed between two fluorinated glass slides separated by 250 μm PTFE spacers. Then the ES (or AT) monomer solution with PEGDA and AIBN was injected into this mold and a second polymerization was conducted under N_2 in a 60^{o}C oven overnight. Unreacted monomers were extracted by washing with DCM, and the ionoelastomer layers were dried at 60 ^{o}C in a vacuum oven to remove residual solvents and water before use.

7. Preparation of polyelectrolyte hydrogels

Two oppositely charged polyelectrolyte hydrogels (K[SPA] and [AETA]Cl) were prepared following a previous report (*20*) with modifications. For polyanion hydrogel (K[SPA]), 3-sulfopropyl acrylate potassium salt (0.6 g) was dissolved in 2.6 mL of DI water (> 18.0 MΩ). Polycationic hydrogel ([AETA]Cl) solution was prepared by dissolving 0.6 g of [2-(acryloyloxy)ethyl]trimethylammonium chloride (Sigma-Aldrich, 496146-200ML) in 3.1 mL of DI water. Then, 10 mol% of purified PEGDA and 0.5 mol% of 2-hydroxy-4'-(2-hydroxyethoxy)-2-methylpropiophenone (I-2959 photoinitiator, Sigma-Aldrich, 410896-10G) were added to the solution and vigorously mixed. Nitrogen gas was sparged in the solutions for 10 min to remove dissolved oxygen. The mixtures were then injected into a glass mold of carbon nanotube/glass and fluorinated-glass separated by 1 mm thick glass spacers. Free radical polymerization was initiated by exposure to UV light (Flood Exposure Source, Newport) for 20 min. After polymerization, free standing hydrogels (1 cm × 1 cm × 1 mm) were peeled off of the substrate and bilayer junction of K[SPA]/K[SPA] and [AETA]Cl/[AETA]Cl were prepared.

8. Dynamic mechanical analysis.

Rheological properties of ionoelastomers were measured by dynamic mechanical analyzer (DMA 850, TA instruments) with uniaxial tensile geometry. ES and AT without carbon nanotube electrodes are prepared in a glass mold of two fluorinated-glasses separated by 500 μm thick PTFE spacers. After polymerization, followed by washing with DCM and drying, ES and AT ionoelastomers were cut into the dimension of 25 mm in length and 5 mm in width. For frequency sweep (**Fig. S5**), 0.01 Hz to 10 Hz oscillational stress were applied with stress amplitude of 4 kPa. We apply 0.1 N pre-load and temperature is maintained at 25 ^{o}C.

9. Thermal analysis

Thermograms of ES and AT were measured by differential scanning calorimetry (Q200, TA instruments). ES and AT ionoelastomers (~15 mg) in standard aluminum DSC pans were heated from - 60 ^{o}C to 40 ^{o}C at a scan rate of 10 ^{o}C/min. Second heating cycle is shown in **Fig. S6A**. TGA of ES and AT were conducted using Q500 (TA instruments). Ionoelastomer samples (~ 15 mg) were heated to 700 ^{o}C at a rate of 10 ^{o}C/min under N_2 condition.

10. Fourier-transform infrared spectroscopy (FTIR)

Attenuated total reflectance (ATR)-FTIR spectrometer (Spectrum 100, PerkinElmer) was used to measure infrared absorption spectra of ionoelastomers.

11. Peel test

To test adhesion, we used a 180° peel test (*33*). Filter paper (Whatman, Grade 1, 180 μm thickness) was cut into pieces of 50 mm in length and 5 mm in width and placed between two fluorinated glass slides separated by 250 μm PTFE spacers. ES (or AT) monomer solutions mixed with 2 mol% PEGDA and 0.5 mol % AIBN were injected into the molds and infiltrated into the filter paper. After polymerization in a 60 °C oven under N_2 overnight and washing unreacted monomers with DCM, led to ionoelastomer layers with filter paper embedded on one side. Then, ES/ES, AT/AT and ES/AT junctions were created by contacting the two ionoelastomers on the faces opposite to the filter paper. The peel test was performed using a tensile testing machine (TA.XT PlusC, Stable Micro Systems) with a rate of 0.1 mm/s. Critical strain energy release rate (G_c) is calculated by $G_c = 2P/W$, where P is the load and W is the sample width.

12. Electrochemical analysis

Unless stated otherwise, the positive terminal (or working electrode) was connected to ES and negative terminal (or counter and reference electrodes) to AT for electrochemical analysis. AC-impedance spectra were measured using a Reference 600^+ instrument (Gamry Instruments) over a frequency range of 1 MHz to 0.1 Hz and an amplitude of 40 mV. A source meter (2635A, Keithley) was used for measuring the current density of ionoelastomer junction as a function of time under various DC biases. Cyclic voltammetry curves with constant voltage ramp and AC current were measured using a Reference 600^+. The input current (or voltage) was generated by a potentiostat (WaveNow, Pine Research Instrumentation).

Cyclic strain of ionoelastomer junctions was induced using a BiSlide positioning motor stage (Velmex). We pre-stretched ES/AT to $\lambda_u = 1.2$ to minimize global buckling during the multiple test cycles. During each cycle, the open circuit voltage (V_{oc}) between working (ES) and counter (AT) electrodes was measured by Gamry Reference 600^+ potentiostat, while the short circuit current (J_{sc}) was separately measured using a Keithley 4200 analyzer. For J_{sc} measurements, the positive and negative electrode leads were shorted together inside the instrument, *i.e.,* the potential drop between ES and AT electrodes was set to zero, and the current flow measured.

Experimental impedance data were fitted using the ZView software (Scribner Associates, version 3.4b). For fitting of ES/AT ionoelatomer junction under DC bias, we performed the fitting by assuming that only the interfacial circuit elements (CPE_{IDL} and R_I) are changed by the external DC biases. The other parameters (R_c, R_B, C_B, and CPE_{EDL}) are fixed to the fitting results under +1V (**Table S3**).

Supplementary Text

1. Equivalent circuit model of ionoelastomer junctions

To analyze AC-impedance result of ES/ES, AT/AT and ES/AT junctions, we adopted the equivalent circuit model used previously (*27*), as shown in the inset of **Fig. 1b**. The model contains a dielectric capacitance (C_B) corresponding to the polarization of the ionic monomer moieties at high frequency. In addition, a resistor (R_B) is connected in parallel that reflects the drift of free ions at moderate frequency. At low frequency, free ions accumulate at the interface resulting in the formation of an electric or ionic double layer that can be described by a constant phase element (CPE). The impedance of a CPE is defined as $Z_{CPE} = Q_\alpha^{-1}(j\omega)^{-\alpha}$ where Q_α is a constant, j is the imaginary number, ω is the angular frequency, and α is a constant ranging from 0 to 1. Another resistor accounting for contact resistance (R_C) is added in series with the equivalent circuit model. In a Nyquist plot of ionoelastomer junctions (**Fig. 1C**), the semi-circle at high frequency corresponds to the parallel connection of R_B and C_B, while the series connection of R_B and CPE results in a tilted line at low frequency. Based on the fitting parameters (**Table S2**), two important variables can be derived—the ionic conductivity (σ) of the ionoelastomers and the capacitance of the EDL (C_{EDL}). First, σ was calculated from the R_B using following equation; $\sigma = \rho^{-1} = \ell A^{-1} R_B^{-1}$, where ρ is the resistivity, ℓ is a thickness of the sample ($\ell = 250 \times 2$ µm) and A is an area ($A = 1$ cm^2). Values of σ for ES/ES and AT/AT homo-junctions are $(1.4 \pm 0.1) \times 10^{-4}$ mS/cm and $(4.2 \pm 0.2) \times 10^{-4}$ mS/cm, respectively, in good agreement with previous reports (*23*). For the ES/AT hetero-junction, an intermediate value of $(2.5 \pm 0.5) \times 10^{-4}$ mS/cm is obtained. On the other hand, effective equivalent EDL capacitance can be estimated from the characteristics of the CPE used in the equivalent circuit model, following the Brug model *(34-36)*: $C_{EDL} = Q_\alpha^{1/\alpha} R_\Omega^{[(1/\alpha)-1]}$ where R_Ω represents the resistive limit of the CPE at $\omega \rightarrow \infty$, herein $R_\Omega = R_B$.

2. Equivalent circuit model of ES/AT junction under DC bias

To reflect the response of the IDL formed at ES/AT junctions to DC bias, we develop a new equivalent circuit model. Two interfacial circuit elements are added: a CPE (CPE_{IDL}) describing the IDL capacitance and a resistor (R_I) accounting for interfacial ionic current. CPE_{IDL} and R_I are connected in parallel and added in series with ES and AT (**Fig. 2F inset**). The Nyquist plot of ES/AT under +1V bias (**Fig. 2F**) shows three different frequency regimes: 1) a semi-circle at high frequency (10 MHz – 800 Hz) corresponding to the parallel connection of R_B and C_B, 2) a second semi-circle at middle frequency (800 Hz –1 Hz) corresponding to the parallel connection of CPE_{IDL} and R_I and 3) a tilted line in the low frequency regime at low frequency (1 Hz – 0.1 Hz) reflecting the series connection of R_C, R_B, CPE_{EDL} and R_I.

Considering that the equivalent circuit model of ES/AT is composed of three impedance components connected in series ($Z = Z_A + Z_B + Z_C$), where Z_A is R_c, Z_B is the total impedance of the series combination of R_B and CPE_{EDL} connected with C_B in parallel, and Z_c is the parallel circuit of CPE_{IDL} and R_I. The impedance of each component can be described as follows:

$$Z_A = R_C, \qquad Z_B = \frac{R_B + Q_{EDL}^{-1}(j\omega)^{-\alpha}}{1 + j\omega R_B C_B + C_B Q_{EDL}^{-1}(j\omega)^{-\alpha+1}}, \qquad Z_C = \frac{R_I Q_{IDL}^{-1}(j\omega)^{-k}}{R_I + Q_{IDL}^{-1}(j\omega)^{-k}} \qquad \text{Eq.2.1}$$

Then, the total impedance (Z) can be expressed as

$$Z = R_C + \frac{R_B + Q_{EDL}^{-1}(j\omega)^{-\alpha}}{1 + j\omega R_B C_B + C_B Q_{EDL}^{-1}(j\omega)^{-\alpha+1}} + \frac{R_I Q_{IDL}^{-1}(j\omega)^{-k}}{R_I + Q_{IDL}^{-1}(j\omega)^{-k}} \qquad \text{Eq.2.2}$$

From the fitting results, we observed that R_I is significantly altered by the applied DC bias (**Fig. S13**). Under forward bias, $R_I \rightarrow 0$. Then, the total impedance (Eq. 2.2) becomes

$$Z_f = R_C + \frac{R_B + Q_{EDL}^{-1}(j\omega)^{-\alpha}}{1 + j\omega R_B C_B + C_B Q_{EDL}^{-1}(j\omega)^{-\alpha+1}} \qquad \text{Eq.2.3}$$

In contrast, under reverse bias, $R_I \rightarrow \infty$. Then, Eq.2.2 becomes

$$Z_r = R_C + \frac{R_B + Q_{EDL}^{-1}(j\omega)^{-\alpha}}{1 + j\omega R_B C_B + C_B Q_{EDL}^{-1}(j\omega)^{-\alpha+1}} + Q_{IDL}^{-1}(j\omega)^{-k} \qquad \text{Eq.2.4}$$

Since C_B is relatively small ($C_B \ll Q_{IDL} \ll Q_{EDL}$, as shown in **Table S3**), and we are interested in the low frequency regime, we can simplify Eq. 2.3 and Eq.2.4 as

$$Z_f \approx R_C + R_B + Q_{EDL}^{-1}(j\omega)^{-\alpha} \qquad \text{Eq.2.5}$$

$$Z_r \approx R_C + R_B + Q_{EDL}^{-1}(j\omega)^{-\alpha} + Q_{IDL}^{-1}(j\omega)^{-k} \qquad \text{Eq.2.6}$$

Since the last term in Eq. 2.6, corresponding to the IDL capacitance represents a much larger impedance than the other three terms, we can see that $Z_r \gg Z_f$, providing the basis of non-Faradaic rectification by the ES/AT ionoelastomer diode.

3. A thermodynamic model for ionoelastomer junctions.

The classical thermodynamic model for electronic p-n semiconductor junctions (*12*) is modified to describe the built-in potential of an ionoelastomer junction. Before the polyanion ES and polycation AT layers are joined, some population of ions are expected to be freely dissociated, while the remainder are associated as neutral aggregates. This dissociation can be described by the following chemical equilibria:

$$ES \underset{K_{ES}}{\Longleftrightarrow} EMIM^{+} + SPA^{-} \qquad \text{Eq. 3.1}$$

$$AT \underset{K_{AT}}{\Longleftrightarrow} AEBI^{+} + TFSI^{-} \qquad \text{Eq. 3.2}$$

We note that there is some disagreement as to the degree of ionization of pure ILs in the literature (*37-39*), but as long as the degree of ionization is not too large, then we can effectively make the following approximation.

The initial concentrations of [EMIM$^+$] and [SPA$^-$] in the ES domain can be written as

$$[EMIM^{+}]^{ES} \approx \sqrt{K_{ES}[ES]}, \qquad [SPA^{-}]^{AT} \approx \sqrt{K_{ES}[ES]} \qquad \text{Eq. 3.3}$$

Similarly, the initial concentrations of [AEBI$^+$] and [TFSI$^-$] in the AT domain can be written as

$$[AEBI^+]^{AT} \approx \sqrt{K_{AT}[AT]}\,, \qquad [TFSI^-]^{AT} \approx \sqrt{K_{AT}[AT]} \qquad \text{Eq. 3.4}$$

After joining ES and AT, the freely dissociated EMIM$^+$ mobile cations from the ES and TFSI$^-$ anions from the AT close to the interface diffuse to mix in a process driven by the entropy and form EMIM$^+$ TFSI$^-$ (ET) IL with dissociation constant K_{ET}.

$$ET \underset{K_{ET}}{\Longleftrightarrow} EMIM^+ + TFSI^- \qquad \text{Eq. 3.5}$$

Diffusion of EMIM$^+$ and TFSI$^-$ leaves behind excess fixed SPA$^-$ charges on the ES side, and excess fixed AEBI$^+$ charges on the AT side, yielding an electric field $\vec{E}$ directed from AT to ES. Since no net current can flow at equilibrium, the current due to the drift of mobile ions in response to the electric field and that due to diffusion must be equal. This balance is described by the Nernst-Planck equation.

$$J = q\left[\underbrace{\mu C(x)E(x)}_{\text{drift}} - \underbrace{D\frac{dC(x)}{dx}}_{\text{diffusion}}\right] = 0 \qquad \text{Eq.3.6}$$

where, μ is the mobility, $C(x)$ is the concentration, D is the diffusion coefficient, and x is the position along the direction perpendicular to the ES/AT interface. Using Einstein's relation $\mu/D = q/k_BT$ and $E(x) = -dV/dx$, eq 3.6 becomes

$$-\frac{q}{k_BT}\frac{dV(x)}{dx} = \frac{1}{C(x)}\frac{dC(x)}{dx} \qquad \text{Eq. 3.7}$$

Boundary conditions are the potential on either side of the IDL (V_{ES} and V_{AT}) and mobile ions concentrations at the edge of IDL region on either side. Integration of eq. 3.7 with those boundary conditions gives eq. 3.8.

$$-\frac{q}{k_BT}\int_{V_{ES}}^{V_{AT}} dV = \int_{[EMIM^+]^{AT}}^{[EMIM^+]^{ES}} \frac{1}{C}dC \quad (EMIM^+\text{cation})$$

$$\text{Eq. 3.8}$$

$$-\frac{q}{k_BT}\int_{V_{ES}}^{V_{AT}} dV = \int_{[TFSI^-]^{ES}}^{[TFSI^-]^{AT}} \frac{1}{C}dC \quad (TFSI^-\text{anion})$$

The potential difference V_{AT} - V_{ES} is the built-in potential V_B, and at the same time, drift and diffusion current from the both cation and anion must be canceled at equilibrium

$$V_B = \frac{k_BT}{q}\ln\frac{[EMIM^+]^{ES}}{[EMIM^+]^{AT}} = \frac{k_BT}{q}\ln\frac{[TFSI^-]^{AT}}{[TFSI^-]^{ES}} = \frac{k_BT}{q}\ln\gamma \qquad \text{Eq.3.9}$$

where γ is the Gibbs-Donnan ratio

$$\gamma = \frac{[EMIM^+]^{ES}}{[EMIM^+]^{AT}} = \frac{[TFSI^-]^{AT}}{[TFSI^+]^{ES}} \qquad \text{Eq.3.10}$$

We assume that a small amount of ET is generated at the interface, resulting in a low concentration of [ET] in both ES and AT, and the initial concentration of majority free ions, *i.e.*, $[\text{EMIM}^+]^{\text{ES}}$ and

[TFSI$^-$]^{AT}, is given by Eq. 3.3 and Eq. 3.4. Then the concentration of minority free ions can be estimated as Eq. 3.11 and Eq. 3.12, respectively.

$$[TFSI^-]^{ES} \approx \frac{K_{ET}}{\sqrt{K_{ES}}}\frac{[ET]}{\sqrt{[ES]}} \qquad \text{Eq.3.11}$$

$$[EMIM^+]^{AT} \approx \frac{K_{ET}}{\sqrt{K_{AT}}}\frac{[ET]}{\sqrt{[AT]}} \qquad \text{Eq.3.12}$$

Using the concentration of majority and minority free ions in Eq. 3.9, then

$$V_B = \frac{k_B T}{q}\ln\frac{\sqrt{K_{ES}K_{AT}}}{K_{ET}}\frac{\sqrt{[ES][AT]}}{[ET]} \qquad \text{Eq.3.13}$$

We can re-write Eq.3.13

$$V_B = V_0 + \frac{k_B T}{q}\ln\frac{\sqrt{[ES][AT]}}{[ET]} \quad \text{where} \quad V_0 = \frac{k_B T}{q}\ln\frac{\sqrt{K_{ES}K_{AT}}}{K_{ET}} \qquad \text{Eq.3.14}$$

Bulk densities of ES and AT were measured to be 1.42 g/cm^3 and 1.50 g/cm^3, respectively, corresponding to [ES] = 4.7 M and [AT] = 3.0 M. We measured V_B of ES/AT ~0.2 V. If K_{ES} and K_{AT} are of a similar magnitude as K_{ET}, then the concentration of ET generated by release of counterions from the interface can be estimated as 1.6×10^{-3} M. We note that this model makes several additional assumptions, including that ET has equal solubility in the two layers, and that the polymer network is unable to intermix even on the length-scale of network strands. Both of these are likely oversimplifications.

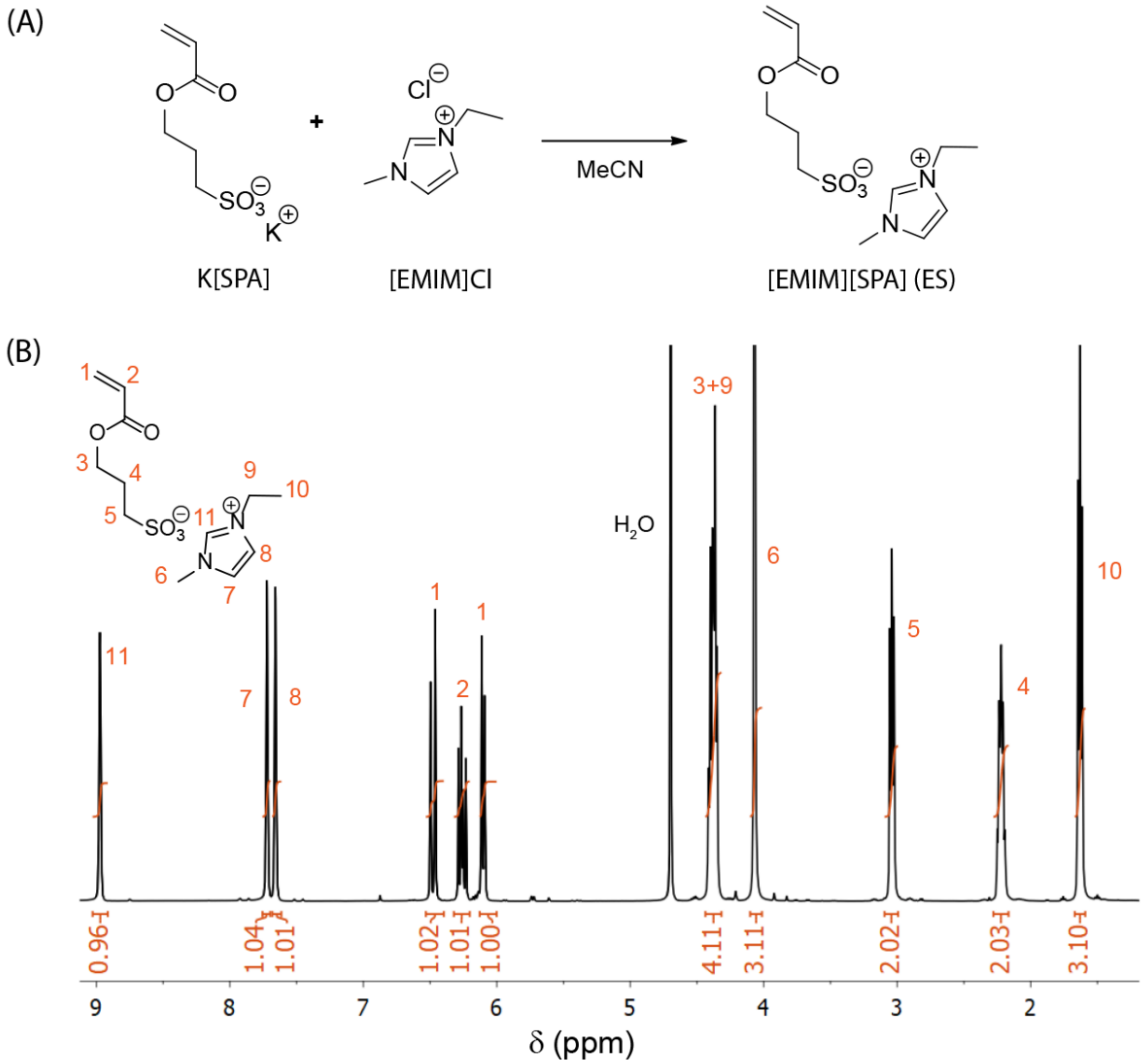

Fig. S1. (**A**) Synthesis scheme and (**B**) ^{1}H- NMR spectra of ES: ^{1}H-NMR (500 MHz, D_2O): 8.61 (s, 1H, H2 (imidazole)), 7.39 (s, 1H, H4 (imidazole)), 7.32 (s, 1H, H5(imidazole)), 6.37-5.88 (m, 3H, CH_2=CH-), 4.21 (t, 2H, CO-O-CH_2-), 4.15-4.11 (m, 2H, N-CH_2-), 3.79 (s, 3H, N-CH_3), 2.94 (t, 2H, -CH_2-S), 2.08-2.03 (m, 2H, CO-O-CH_2-CH_2-), 1.40 (t, 3H, N-CH_2-CH_3).

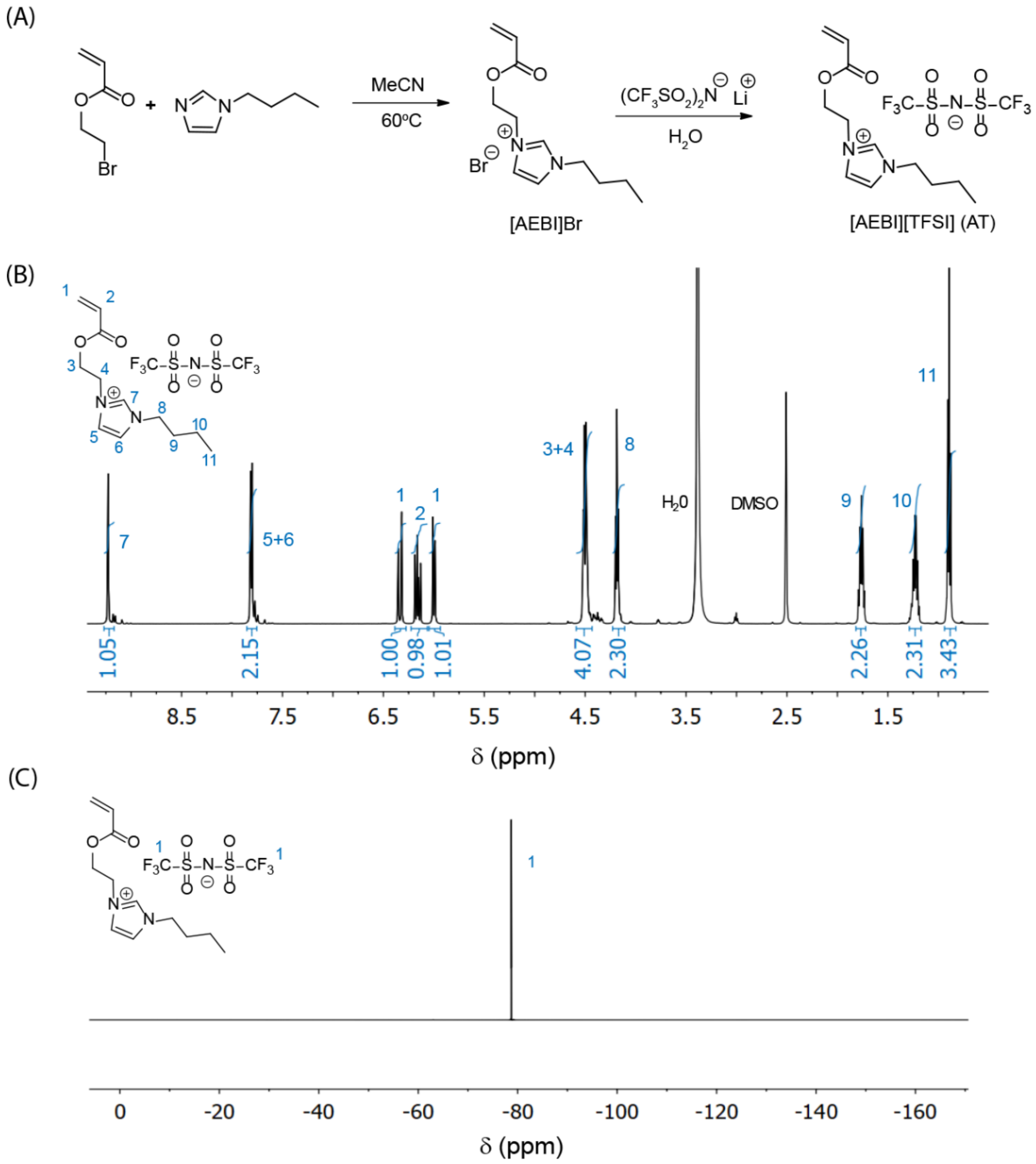

Fig. S2. (**A**) Synthetic scheme of AT and (**B**) ^{1}H- and (C) ^{19}F-NMR of AT: ^{1}H-NMR(500 MHz, D$_6$-DMSO): 9.23 (s, 1H, H2 (imidazole)), 7.81 (d, 2H, H4 H5 (imidazole)), 6.35-5.99 (m, 3H, CH_2=CH-), 4.51-4.49 (m, 4H, CO-O-CH_2-CH_2), 4.19 (t, 2H, N-CH_2-), 1.79-1.73 (m, 2H, N-CH_2-CH_2), 1.25-1.20 (m, 2H, N-CH_2-CH_2-CH_2-), 0.89 (t, 3H, -CH_3) and ^{19}F-NMR(500 MHz, D$_6$-DMSO): δ =79.9 (s, 6F, -CF_3).

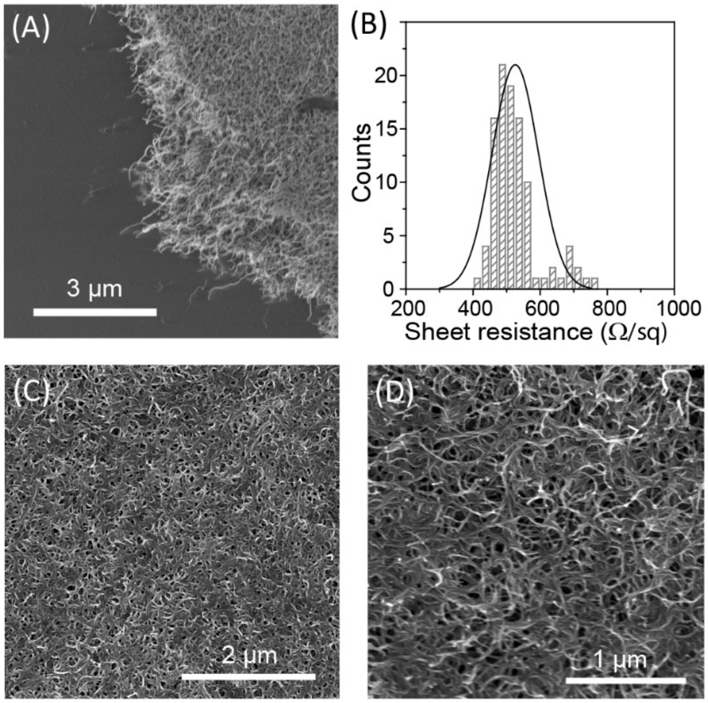

Fig. S3. SEM images of (**A**) a glass substrate coated by carbon nanotubes. (**B**) distribution of sheet resistance (mean value = 525 ± 69 Ω/sq) in the carbon nanotube coated glass substrate (2.5 cm x 4 cm), as measured by a four-point probe method with total number of measurements = 100. SEM images of the carbon nanotube-containing sides of (**B**) ES and (**C**) AT layers showing transfer from the glass substrate to both ionoelastomers.

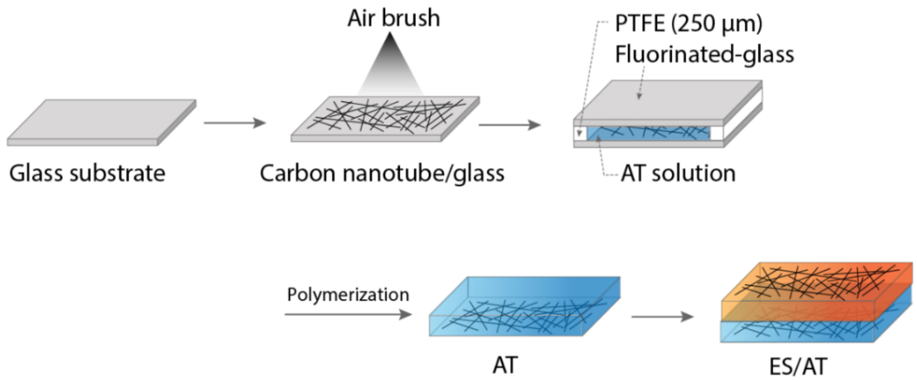

Fig. S4. Schematic illustration of the preparation of ES/AT junctions. A layer of 8% carboxylic functionalized carbon nanotubes was first deposited on a glass substrate using an air-brush method. AT (or ES) was mixed with 2 mol% PEGDA as a crosslinker and 0.5 mol% AIBN as an initiator. The viscous mixture was then injected into a sandwiched glass mold of carbon nanotubes/glass and fluorinated-glass separated by 250 µm thick poly(tetrafluoroethylene) spacers. Polymerization of the mixture was conducted under N_2 at 60 ^oC. After polymerization, ES/AT was obtained by simply attaching the two bare surfaces of ES and AT.

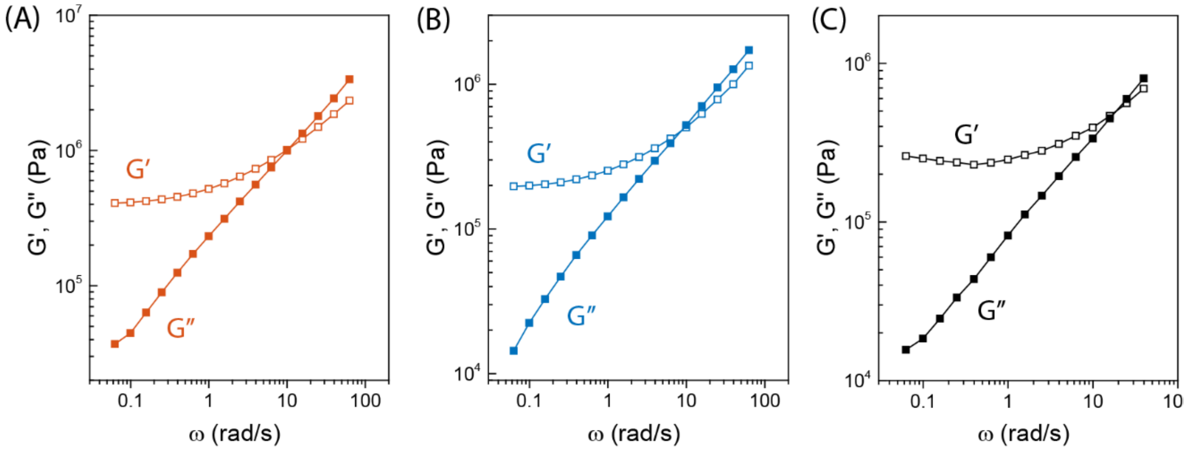

Fig. S5. Dynamic storage (G′) and loss (G″) moduli of (**A**) ES and (**B**) AT ionoelastomers and (**C**) ES/AT heterojunction. For all samples, typical rheological characteristics of lightly-crosslinked elastomers are observed, as indicated by weakly frequency dependent rubbery plateaus in G′ at low frequencies ($\omega < 10$ rad/s), and glass transition region ($\omega > 10$ rad/s) with slightly higher G″ than G′. The chain relaxation time (τ_c) is estimated by $\tau_c=2\pi/\omega_0$, where ω_0 is the frequency at the cross point of G′ and G″, and similar τ_c of 0.6 s is estimated for ES and AT ionoelastomers and ES/AT heterojunction.

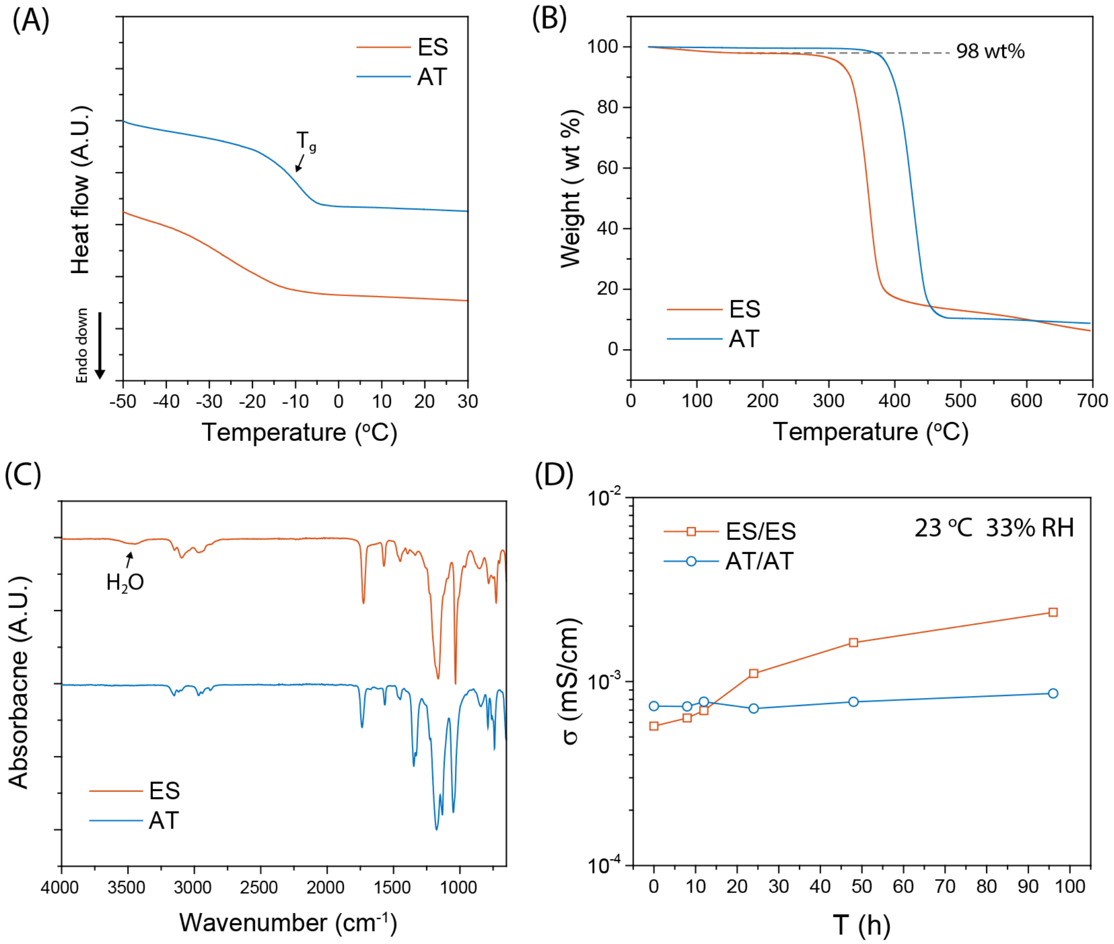

Fig. S6. **(A)** The second heating cycle of differential scanning calorimetry (DSC) thermograms for ES and AT ionoelastomers with a heating rate of 10 °C/min. The glass transitions of ES and AT are observed at temperatures of -20 °C and -10 °C, respectively. **(B)** Thermogravimetric analysis (TGA) of ionoelastomers with a heating rate of 10 °C/min. A small amount of residual water in ES can be seen from the ≈ 2 wt% weight loss at 100 °C. **(C)** The vibration peak of water molecules in the range of 3300 - 3500 cm^{-1} is observed for ES in attenuated total reflectance Fourier transform infrared spectroscopy (ATR-FTIR). **(D)** Ion conductivity (σ) changes of ES/ES and AT/AT stored at 23 °C and 33% RH.

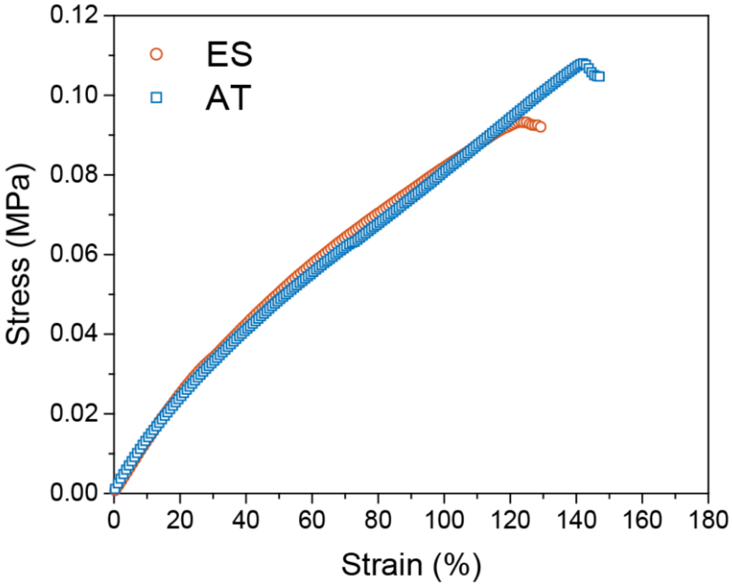

Fig. S7. Stress-strain curves of ES and AT. Young's modulus of ES and AT are measured to be 100 kPa, along with the elongations at break of ~120 % for ES and ~140% for AT.

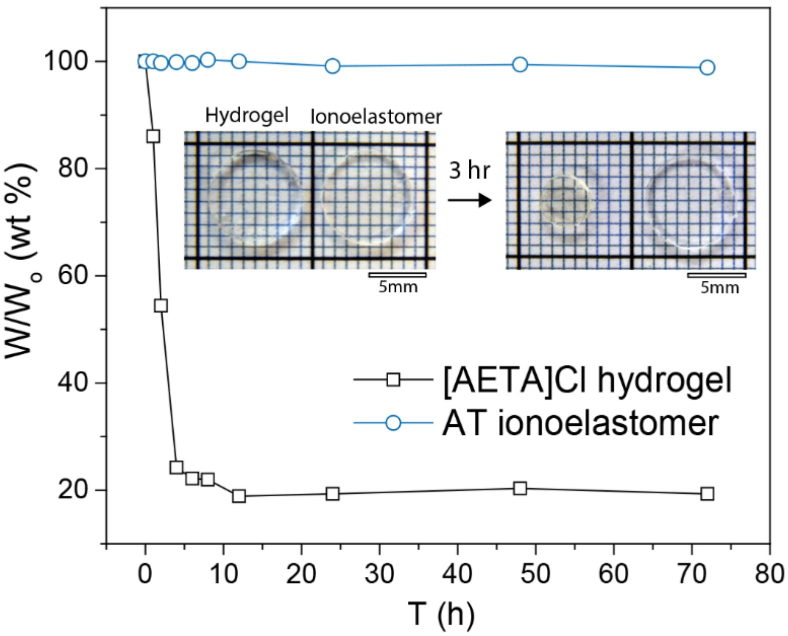

Fig. S8. Weight loss of ionoelastomer and hydrogel layers in ambient conditions. The weight of [AETA]Cl hydrogels rapidly decreases below 20 wt% after 6 h. In stark contrast, no weight changes are observed from the ionoelastomer. The insets show photographs of the [AETA]Cl hydrogel and AT ionoelastomers stored in ambient conditions.

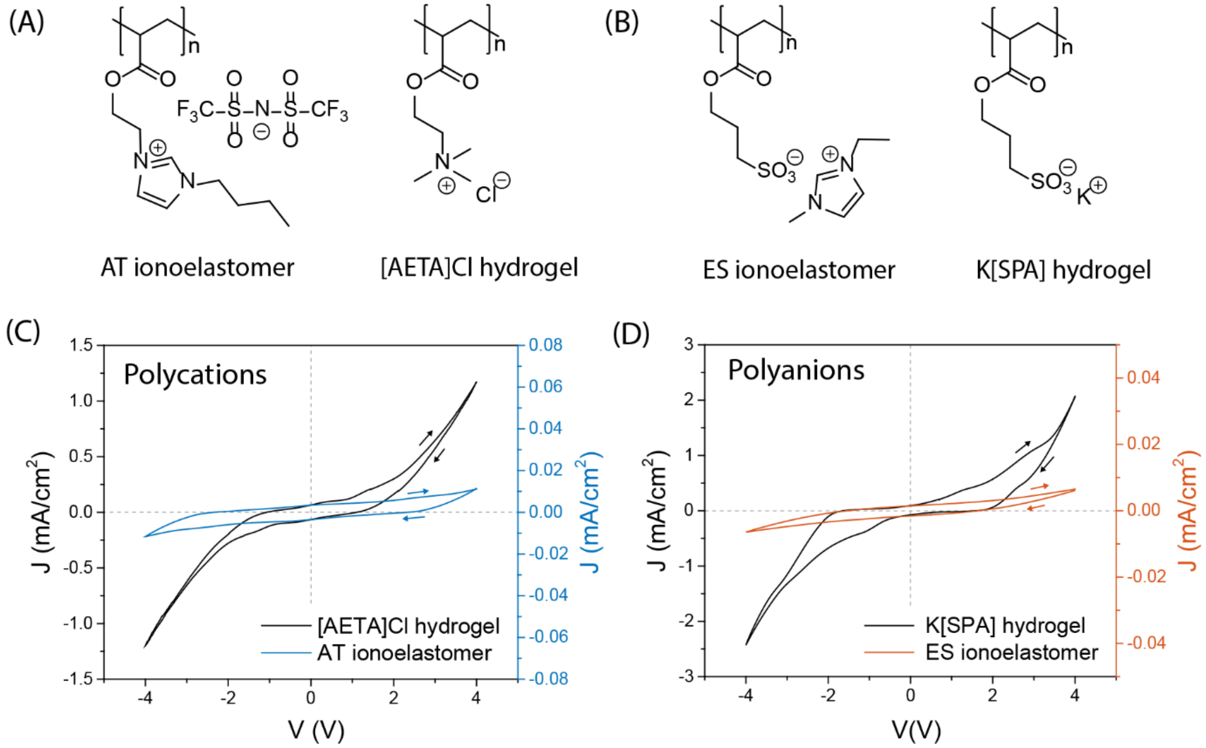

Fig. S9. Electrochemical window of ionoelastomers and polyelectrolyte hydrogels with carbon nanotube electrodes. Chemical structures of (**A**) polycationic AT ionoelastomer and [AETA]Cl hydrogel and (**B**) polyanionic ES ionoelastomer and K[SPA] hydrogel. To measure the electrochemical window, cyclic voltammetry curves of (**C**) polycations and (**D**) polyanions are measured with the voltage scan rate of 5 mV/s. Both hydrogels undergo electrochemical redox reactions less than ± 1 V, resulting in a rapid increase of slope in current density, while ionoelastomers show wider electrochemical window of about ± 3 V.

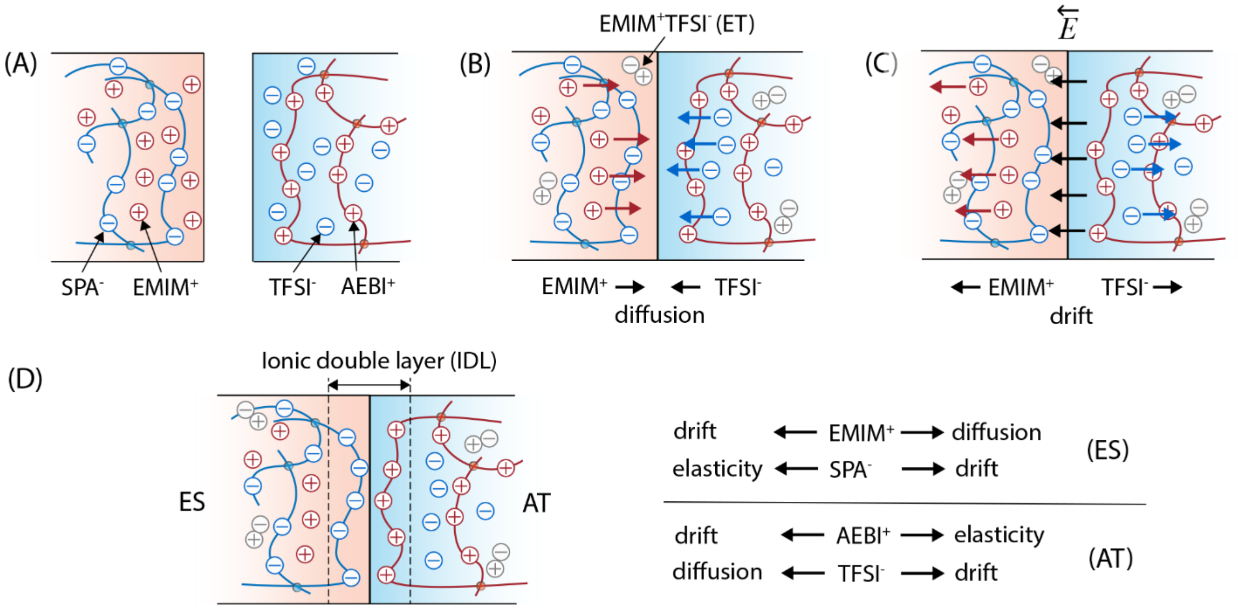

Fig. S10. Ionoelastomers form a heterojunction by balancing two concurrent processes: the diffusion of mobile ions due to the entropy of mixing, and the drift of mobile ions due to the electric field of the excess polyions. (**A**) In an ES ionoelastomer, some of the EMIM$^+$ cations dissociate from the SPA$^-$ polyanions. In an AT ionoelastomer, some of the TFSI$^-$ anions dissociate from the AEBI$^+$ polycations. (**B**) When the two ionoelastomers are brought into contact, the entropy of mixing drives the dissociated EMIM$^+$ cations to diffuse from ES into AT, and drives the dissociated TFSI$^-$ anions to diffuse from AT into ES. Near the interface, the mobile EMIM$^+$ and TFSI$^-$ form an ionic liquid (ET). The entropic depletion of mobile ions leaves behind excess SPA$^-$ polyanion chains on the ES side, and excess AEBI$^+$ polycation chains on the AT side. By contrast, the polyion chains are restrained by the crosslinked networks and do not undergo long-range motion. (**C**) These excess fixed charges yield an electric field directed from AT to ES, leading to a drift current of the mobile ions in the direction opposite to their diffusion current. (**D**) At equilibrium, the drift currents balance the diffusion currents, leading to a depletion of mobile ions from the interface and corresponding double layer of fixed ions.

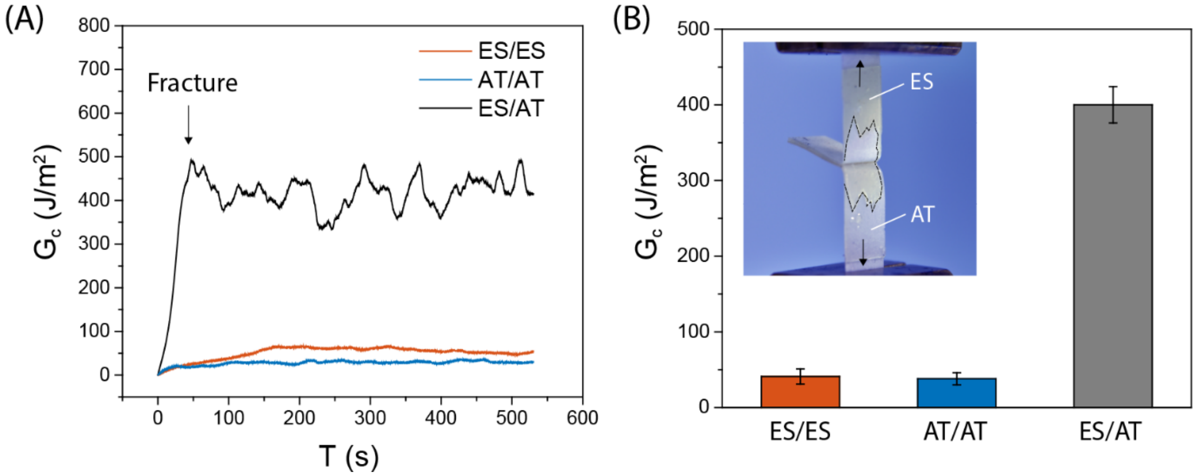

Fig. S11. (**A**) Critical strain energy release rate (G_c) of ES/ES (red) and AT/AT (blue) homojunctions and ES/AT (black) heterojunction during the peel test. ES/ES and AT/AT homojunctions peel easily along the interface but peeling of ES/AT heterojunction leads to cohesive failure. (**B**) Average G_c value from the peel test (number of samples = 5). Inset shows a photograph of peel test of an ES/AT junction, showing cohesive failure due to strong adhesion of the ES/AT interface.

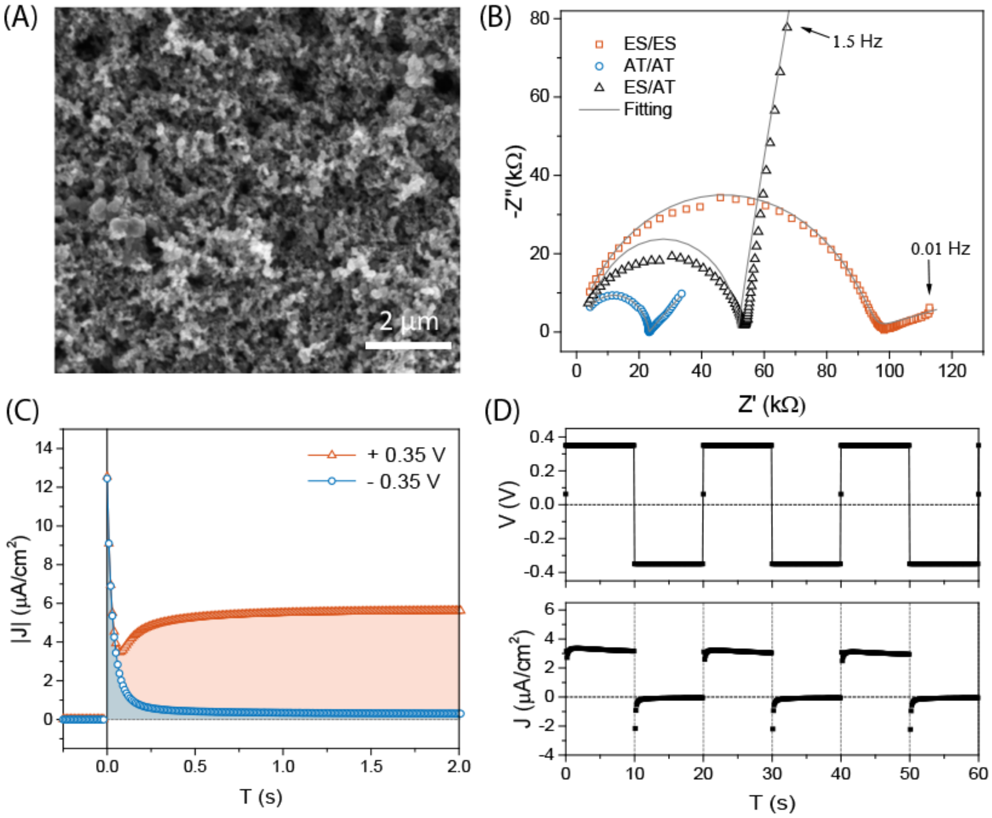

Fig. S12. (**A**) SEM images of microporous layer (MPL) carbon electrodes. (**B**) Nyquist plot of AC-impedance measurement of ES/ES, AT/AT and ES/AT ionoelastomer junctions with MPL carbon electrodes. Gray lines represent fits of the equivalent circuit model shown in the inset of Fig. 1D. Capacitance values for ES/ES and AT/AT homojunctions from the fittings are 4.1 ± 0.3 mF/cm^2 and 2.1 ± 0.4 μF/cm^2, respectively; these values are roughly one order of the magnitude larger than the ~ 0.1 mF/cm^2 values with carbon nanotubes, while the capacitance value for ES/AT remains the similar ~ 1 μF/cm^2. (**C**) Current density of an ES/AT junction under forward bias of +0.35 V and reverse bias of -0.35 V, applied at 0 s. The total associated charges (Q) determined by integrating the current density curves are $Q_f = 0.6 \pm 0.1$ mC/cm^2 and $Q_r = 1.1 \pm 0.3$ μC/cm^2. (**D**) Rectification by ionoelastomer junctions with MPL electrodes under the alternating potential of ± 0.35 V at a frequency of 0.05 Hz.

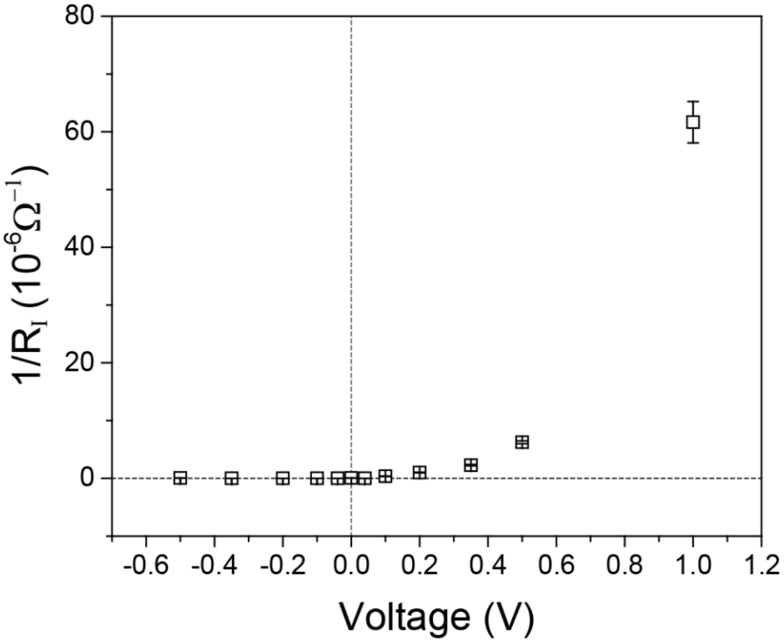

Fig. S13. Inverse of interfacial resistances (R_I) determined by the fitting the AC-impedance data for ES/AT interface under DC bias using the equivalent circuit model shown in Fig 2F. We performed the fitting by assuming only interfacial circuit elements (CPE_{IDL} and R_I) are changed by the external DC biases while the other parameters (R_c, R_B, C_B, and CPE_{EDL}) are fixed using the fitting results under +1V shown in Table S3.

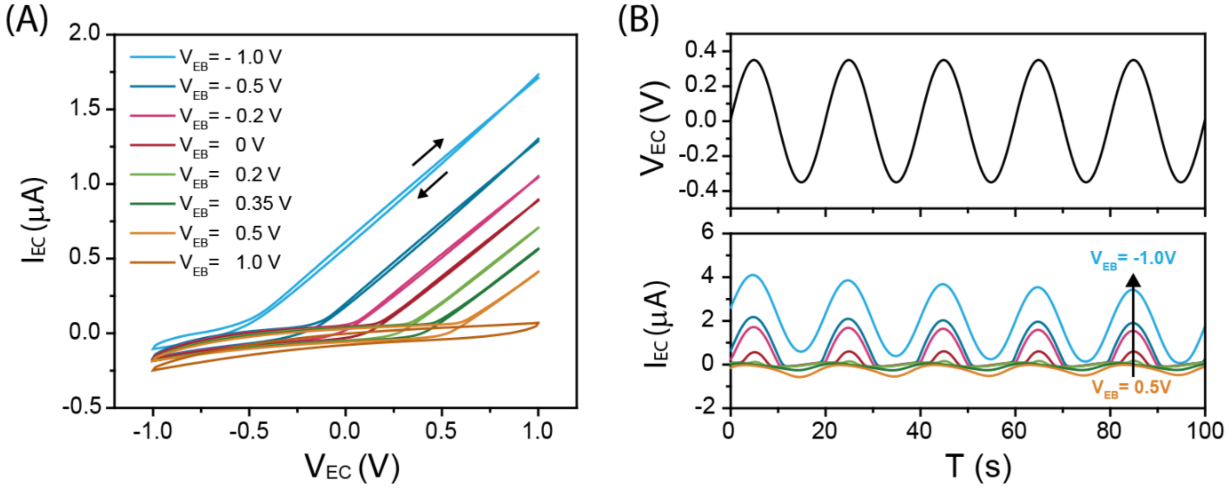

Fig. S14. (**A**) Output characteristic (I_{EC}-V_{EC}) curves of ES/AT/ES ionoelastomer transistor, operated with voltage input (V_{EB}). Cyclic potential sweeps from V_{EC} = -1 V to 1 V with a constant rate of 0.1V/s were applied. (**B**) Switching characteristics of ES/AT/ES device under 0.05 Hz AC potential with 0.35 V amplitude.

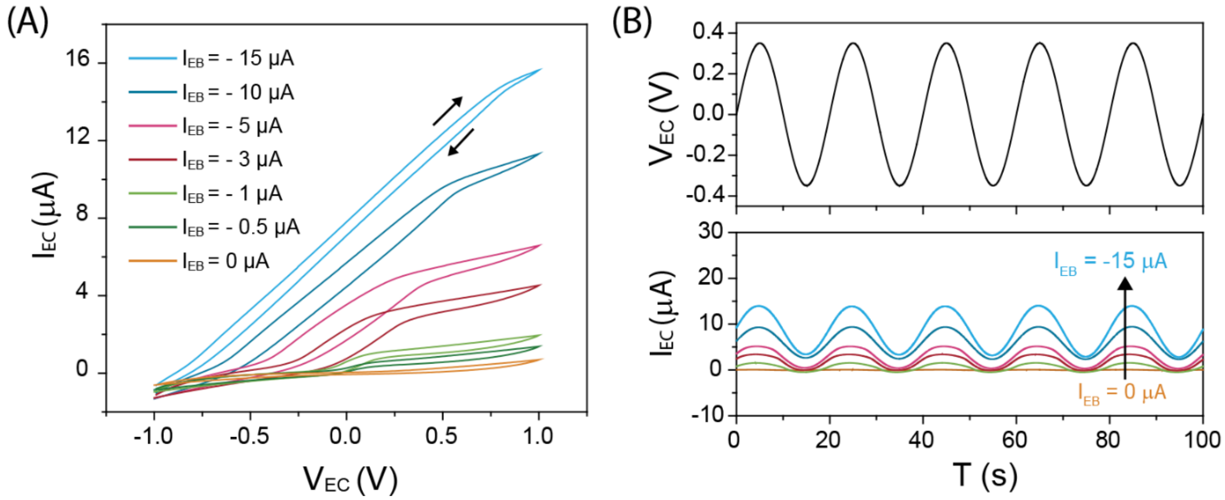

Fig. S15. (**A**) Output characteristic (I_{EC}-V_{EC}) curves of ES/AT/ES ionoelastomer transistor with microporous carbon electrode, operated with current input (I_{EB}). (**B**) Switching characteristics of ES/AT/ES device under 0.05 Hz AC potential with 0.35 V amplitude. On-off ratio of root mean square currents between the on ($I_{EB} \leq -15$ μA) and off ($I_{EB} \geq 0$ μA) states is measured to be ≈ 150.

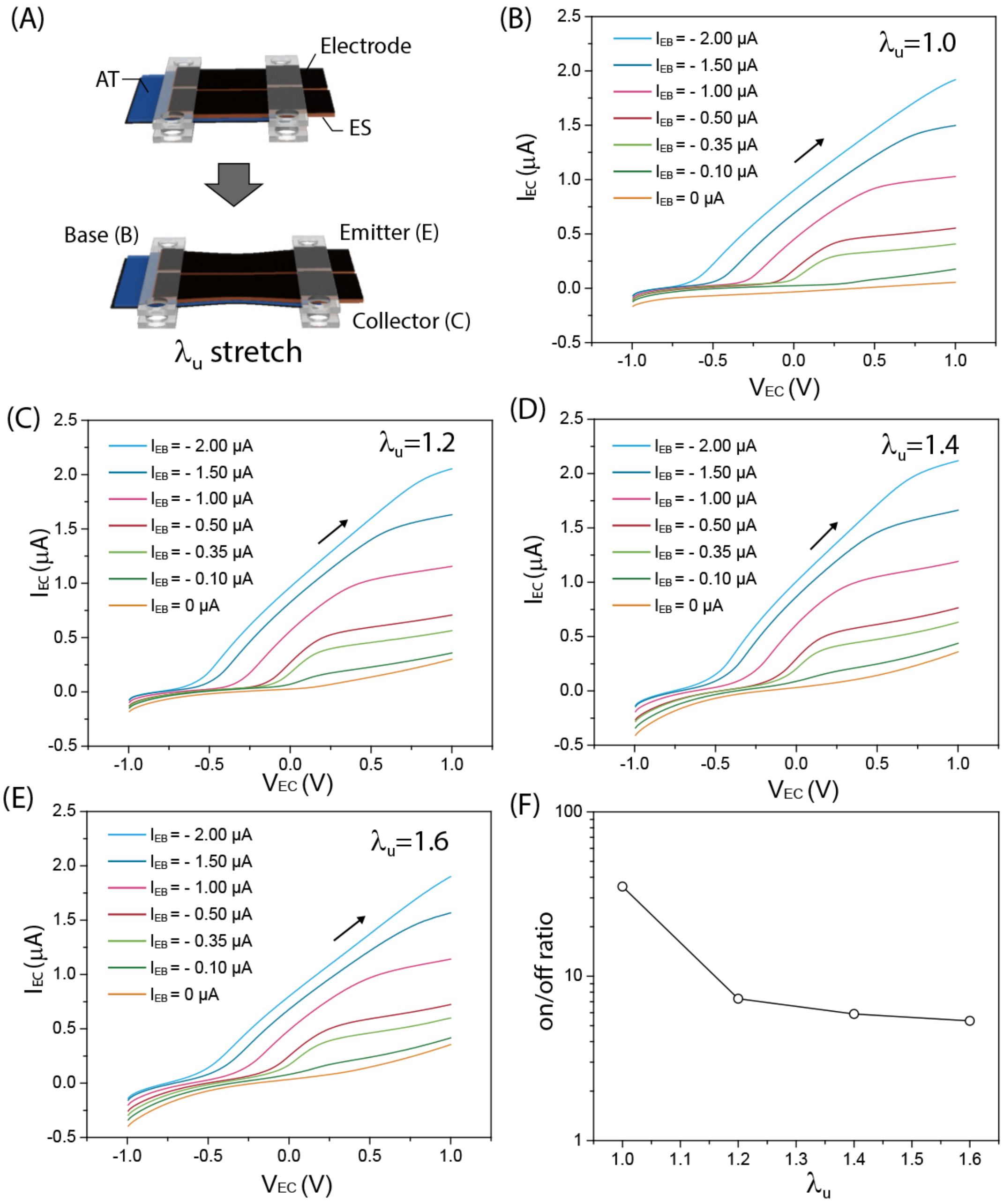

Fig. S16. (A) Schematic illustration of an ES/AT/ES ionoelastomer transistor and uniaxial stretching of the transistor. Output characteristic (I_{EC}-V_{EC}) curves operated with different uniaxial stretch ratio of **(B)** $\lambda_u = 1.0$, **(C)** $\lambda_u = 1.2$, **(D)** $\lambda_u = 1.4$, and **(E)** $\lambda_u = 1.6$. **(F)** On-off ratio ($= I_{EC}^{on}/I_{EC}^{off}$, where I_{EC}^{on} is on-current at $I_{EB} = -2\ \mu A$ and $V_{EB} = 1V$, and I_{EC}^{off} is off-current at $I_{EB} = 0\ \mu A$ and $V_{EB} = 1V$) is plotted as a function of stretching ratio λ_u

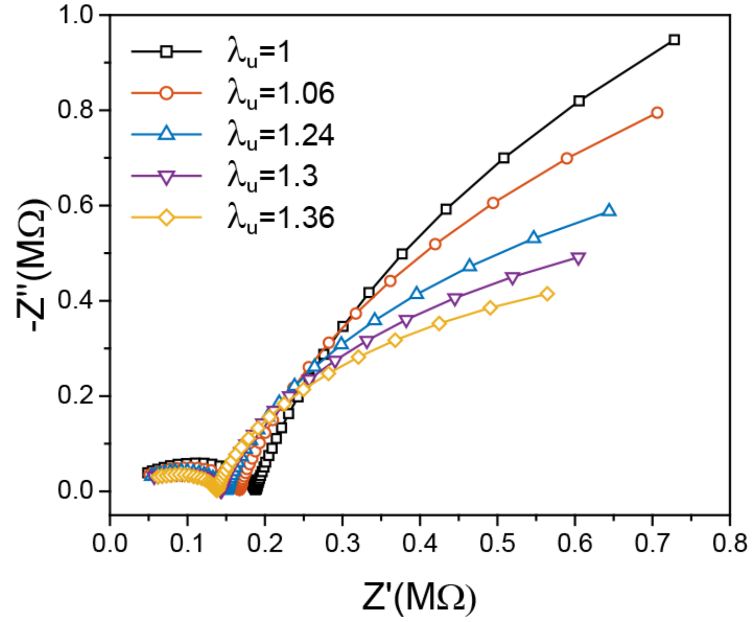

Fig. S17. Nyquist plot of for an ES/AT ionoelastomer junction uniaxially stretched by a factor of λ_u.

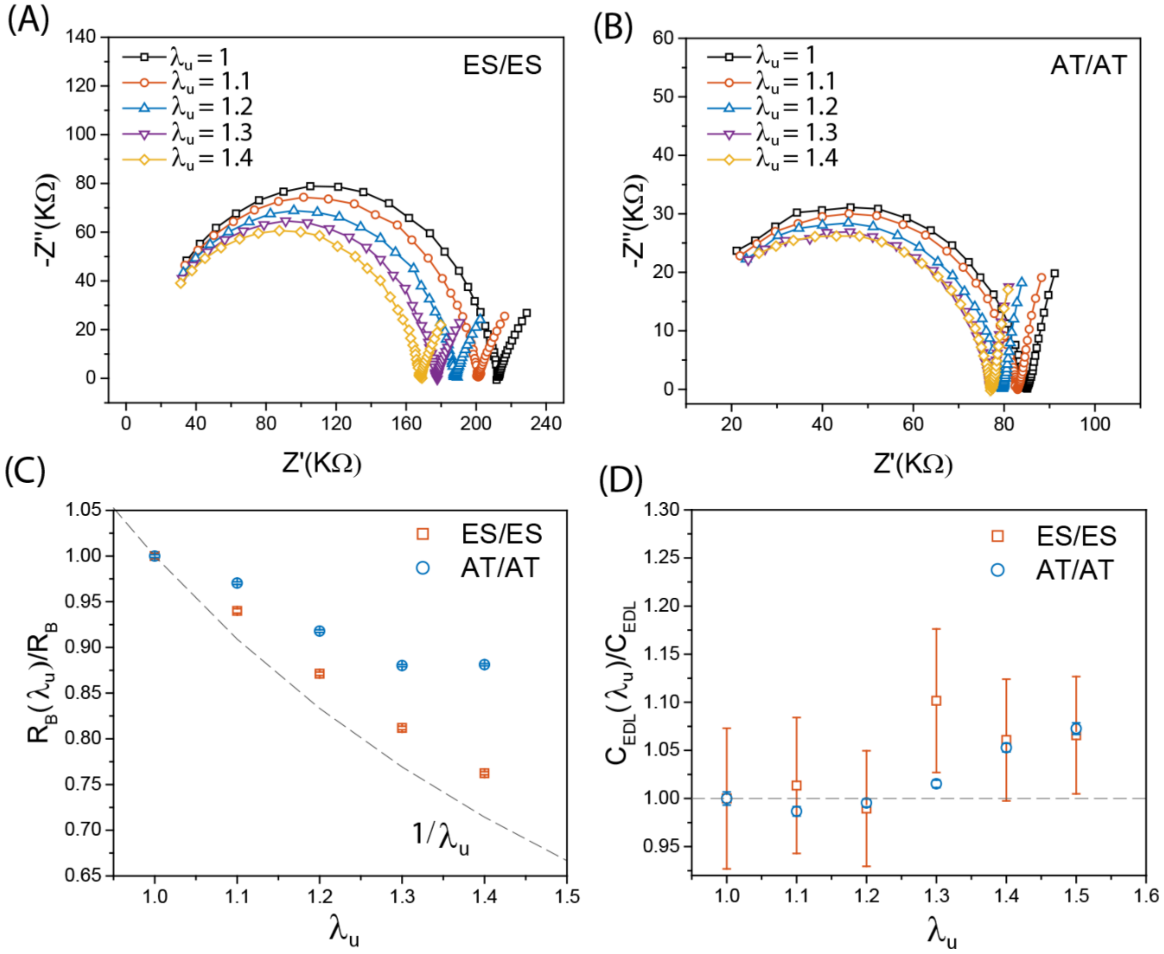

Fig. S18. Nyquist curves of (**A**) ES/ES and (**B**) AT/AT with uniaxial stretching by a factor of λ_u, and corresponding (**C**) $R_B(\lambda_u)$ and (**D**) $C_{EDL}(\lambda_u)$. While ES/ES and AT/AT homo-junctions showed a $1/\lambda_u$ decrease of $R_B(\lambda_u)$ in good agreement with expectations, both C_{EDL} remained nearly constant because there was no actual area increase of the ES/carbon nanotube and AT/carbon nanotube interfaces as the devices were stretched.

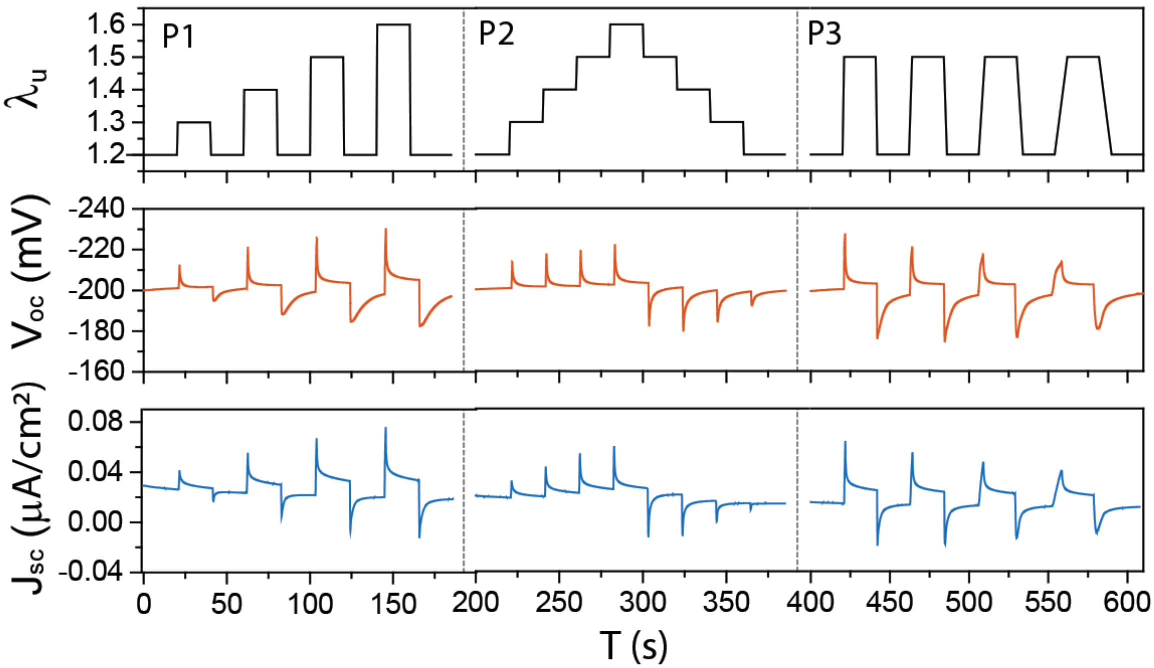

Fig. S19. Electromechanical response of ES/AT ionoelastomer junctions under various deformation programs. P1: different magnitude of uniaxial stretching from $\lambda_u = 1.2$ to $\lambda_u = 1.3$, 1.4, 1.5 and 1.6 with displacement rates of 3 mm/s, 6 mm/s, 9 mm/s and 12 mm/s, respectively. P2: step increase by 0.1 from $\lambda_u = 1.2$ to 1.6 with a displacement of rate of 3 mm/s. P3: uniaxial stretching from $\lambda_u = 1.2$ to $\lambda_u = 1.5$ with displacement rates of 9 mm/s, 4.5 mm/s, 1.5 mm/s, 0.38 mm/s, respectively.

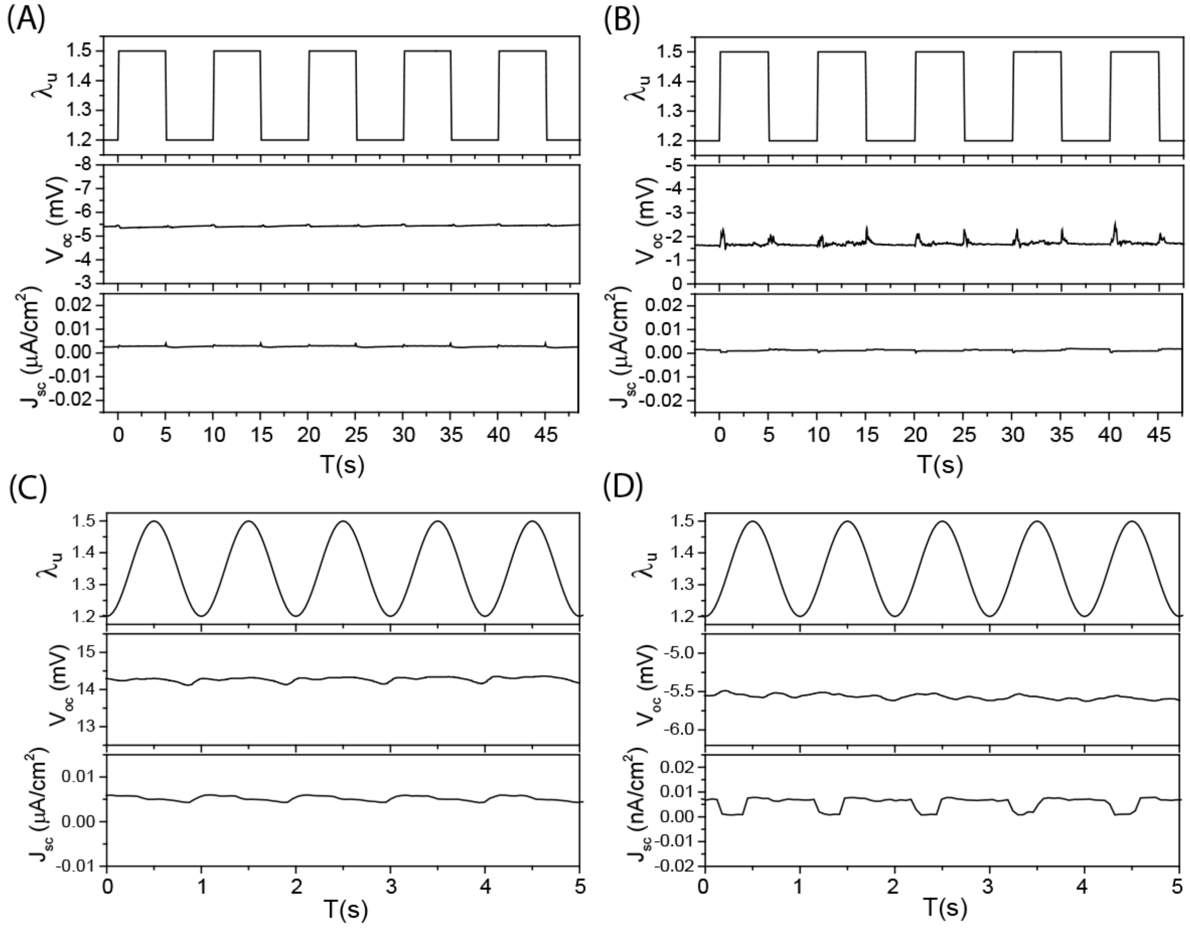

Fig. S20. V_{oc} and J_{sc} generated by (**A**) ES/ES and (**B**) AT/AT under 0.05 Hz of cyclic step strain with the displacement rate of 12 mm/s. Electric response of (**C**) ES/ES and (**D**) AT/AT under 1 Hz sinusoidal strain. ES/ES and AT/AT interfaces generated negligible electrical signals ($\Delta V_{oc} <$ 1 mV and $\Delta J_{sc} <$ 5 nA/cm^2).

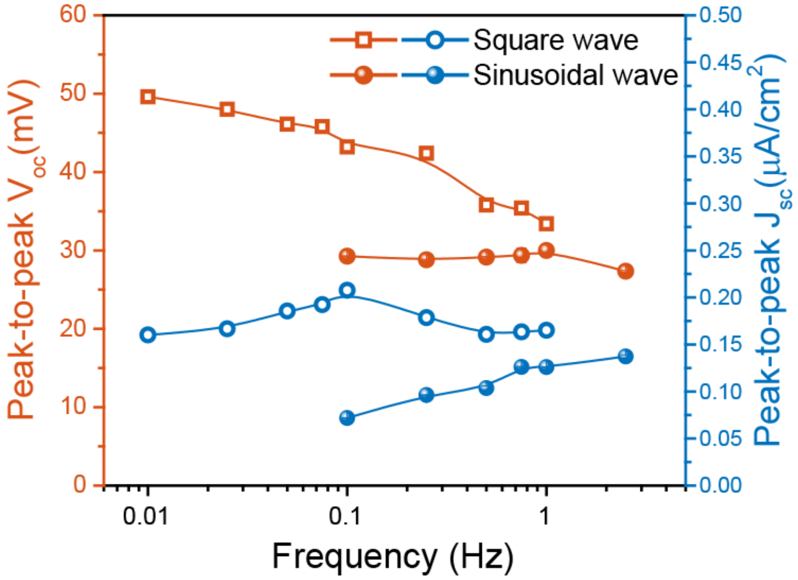

Fig. S21. Peak-to-peak V_{oc} (red) and J_{sc} (blue) responses generated by ES/AT at various operating frequencies.

Table S1. Weight increase and sheet resistance for air-brush coated layers of carbon nanotubes, and capacitance of EDL from homojunction of ES/ES and AT/AT

Amount of spraying	Weight increase[a)]	Sheet resistance [b)]	C_{EDL} of ES/ES [c)]	C_{EDL} of AT/AT [d)]
1 mL	< 0.3 mg	1413 ± 192 Ω/sq	$(8.2 \pm 1.0) \times 10^{-5}$ F/cm^2	$(9.4 \pm 0.8) \times 10^{-5}$ F/cm^2
2.5 mL	0.4 ± 0.2 mg	958 ± 113 Ω/sq	$(1.2 \pm 0.5) \times 10^{-4}$ F/cm^2	$(7.3 \pm 1.0) \times 10^{-5}$ F/cm^2
5 mL	0.7 ± 0.3 mg	549 ± 27 Ω/sq	$(1.5 \pm 0.3) \times 10^{-4}$ F/cm^2	$(1.0 \pm 0.2) \times 10^{-4}$ F/cm^2
10 mL	1.0 ± 0.8 mg	407 ± 22 Ω/sq	$(2.6 \pm 0.3) \times 10^{-4}$ F/cm^2	$(1.5 \pm 0.3) \times 10^{-4}$ F/cm^2

[a)] Average of 5 different samples. [b)] 10 measurements for each of 5 different samples. [c,d)] 250 μm thick ES and AT layers are prepared on the carbon nanotube coated-glass substrates and capacitance of EDL from ES/ES and AT/AT homojunctions are measured by AC-impedance using the circuit model shown in Fig. 1.

Table S2. AC-impedance fitting parameters for ES/ES, AT/AT and ES/AT shown in Fig. 2C and 2D.

	R_C (kΩ)	R_B (kΩ)	CPE		C_B (pF)
			Q_α	α	
ES/ES	26.2 ± 1.2	170.8 ± 1.7	$(3.9 \pm 0.3)\times10^{-5}$	0.54 ± 0.05	46.1 ± 1.0
AT/AT	28.3 ± 2.6	56.2 ± 0.7	$(7.2 \pm 0.1)\times10^{-5}$	0.79 ± 0.01	55.7 ± 1.5
ES/AT	23.1 ± 0.9	102.2 ± 1.1	$(9.5 \pm 0.1)\times10^{-7}$	0.83 ± 0.01	62.6 ± 1.7

Table S3. Fitting parameters for the circuit components in the equivalent circuit model for IDL under +1 V of forward bias.

	R_C (kΩ)	R_B (kΩ)	CPE_{EDL}		C_B (pF)	CPE_{IDL}		R_I (kΩ)
			Q_{EDL}	α		Q_{IDL}	k	
ES/AT +1V	22.9 ± 0.8	59.6 ± 0.8	$(1.3 \pm 0.1) \times 10^{-4}$	0.71 ± 0.09	47.3 ± 1.5	$(4.0 \pm 1.3) \times 10^{-7}$	0.89 ± 0.06	16.2 ± 1.0

Table S4. ES/AT electromechanical transducer devices under 1Hz sinusoidal stretching from λ_u = 1.2 to λ_u = 1.5

Sample #	#1	#2	#3	#4	#5	#6	#7	#8	average
Peak-to-peak V_{oc} (mV)	35	35	36	37	41	45	34	38	37 ± 3
Peak-to-peak J_{sc} ($\mu A/cm^2$)	0.22	0.15	0.30	0.19	0.20	0.18	0.23	0.12	0.20 ± 0.05

References and Notes

1. C. Yang, Z. Suo, Hydrogel ionotronics. *Nat. Rev. Mater.* **3**, 125–142 (2018). doi:10.1038/s41578-018-0018-7

2. C. Keplinger, J.-Y. Sun, C. C. Foo, P. Rothemund, G. M. Whitesides, Z. Suo, Stretchable, transparent, ionic conductors. *Science* **341**, 984–987 (2013). doi:10.1126/science.1240228 Medline

3. B. Chen, J. J. Lu, C. H. Yang, J. H. Yang, J. Zhou, Y. M. Chen, Z. Suo, Highly stretchable and transparent ionogels as nonvolatile conductors for dielectric elastomer transducers. *ACS Appl. Mater. Interfaces* **6**, 7840–7845 (2014). doi:10.1021/am501130t Medline

4. Y. Hou, Y. Zhou, L. Yang, Q. Li, Y. Zhang, L. Zhu, M. A. Hickner, Q. M. Zhang, Q. Wang, Flexible Ionic Diodes for Low-Frequency Mechanical Energy Harvesting. *Adv. Energy Mater.* **7**, 1601983 (2017). doi:10.1002/aenm.201601983

5. H.-R. Lee, C.-C. Kim, J.-Y. Sun, Stretchable Ionics - A Promising Candidate for Upcoming Wearable Devices. *Adv. Mater.* **30**, e1704403 (2018). doi:10.1002/adma.201704403 Medline

6. H. Chun, T. D. Chung, Iontronics. *Annu. Rev. Anal. Chem.* **8**, 441–462 (2015). doi:10.1146/annurev-anchem-071114-040202 Medline

7. C.-C. Kim, H.-H. Lee, K. H. Oh, J.-Y. Sun, Highly stretchable, transparent ionic touch panel. *Science* **353**, 682–687 (2016). doi:10.1126/science.aaf8810 Medline

8. C. H. Yang, B. Chen, J. J. Lu, J. H. Yang, J. Zhou, Y. M. Chen, Z. Suo, Ionic cable. *Extreme Mech. Lett.* **3**, 59–65 (2015). doi:10.1016/j.eml.2015.03.001

9. C. Larson, B. Peele, S. Li, S. Robinson, M. Totaro, L. Beccai, B. Mazzolai, R. Shepherd, Highly stretchable electroluminescent skin for optical signaling and tactile sensing. *Science* **351**, 1071–1074 (2016). doi:10.1126/science.aac5082 Medline

10. O. Kim, S. J. Kim, M. J. Park, Low-voltage-driven soft actuators. *Chem. Commun.* **54**, 4895–4904 (2018). doi:10.1039/C8CC01670D Medline

11. T. Li, G. Li, Y. Liang, T. Cheng, J. Dai, X. Yang, B. Liu, Z. Zeng, Z. Huang, Y. Luo, T. Xie, W. Yang, Fast-moving soft electronic fish. *Sci. Adv.* **3**, e1602045 (2017). doi:10.1126/sciadv.1602045 Medline

12. B. G. Streetman, *Solid State Electronic Devices* (Prentice Hall, 1990).

13. B. Lovrecek, A. Despic, J. O. M. Bockris, Electrolytic Junctions with Rectifying Properties. *J. Phys. Chem.* **63**, 750–751 (1959). doi:10.1021/j150575a030

14. S. Mafé, P. Ramírez, Electrochemical characterization of polymer ion-exchange bipolar membranes. *Acta Polym.* **48**, 234–250 (1997). doi:10.1002/actp.1997.010480702

15. B. Yameen, M. Ali, R. Neumann, W. Ensinger, W. Knoll, O. Azzaroni, Single conical nanopores displaying pH-tunable rectifying characteristics. manipulating ionic transport with zwitterionic polymer brushes. *J. Am. Chem. Soc.* **131**, 2070–2071 (2009). doi:10.1021/ja8086104 Medline

16. I. Vlassiouk, T. R. Kozel, Z. S. Siwy, Biosensing with nanofluidic diodes. *J. Am. Chem. Soc.* **131**, 8211–8220 (2009). doi:10.1021/ja901120f Medline

17. J.-H. Han, K. B. Kim, H. C. Kim, T. D. Chung, Ionic circuits based on polyelectrolyte diodes on a microchip. *Angew. Chem. Int. Ed.* **48**, 3830–3833 (2009). doi:10.1002/anie.200900045 Medline

18. T. B. H. Schroeder, A. Guha, A. Lamoureux, G. VanRenterghem, D. Sept, M. Shtein, J. Yang, M. Mayer, An electric-eel-inspired soft power source from stacked hydrogels. *Nature* **552**, 214–218 (2017). doi:10.1038/nature24670 Medline

19. O. J. Cayre, S. T. Chang, O. D. Velev, Polyelectrolyte diode: Nonlinear current response of a junction between aqueous ionic gels. *J. Am. Chem. Soc.* **129**, 10801–10806 (2007). doi:10.1021/ja072449z Medline

20. H.-R. Lee, J. Woo, S. H. Han, S.-M. Lim, S. Lim, Y.-W. Kang, W. J. Song, J.-M. Park, T. D. Chung, Y.-C. Joo, J.-Y. Sun, A Stretchable Ionic Diode from Copolyelectrolyte Hydrogels with Methacrylated Polysaccharides. *Adv. Funct. Mater.* **29**, 1806909 (2018). doi:10.1002/adfm.201806909

21. K. Tybrandt, R. Forchheimer, M. Berggren, Logic gates based on ion transistors. *Nat. Commun.* **3**, 871 (2012). doi:10.1038/ncomms1869 Medline

22. K. Tybrandt, K. C. Larsson, A. Richter-Dahlfors, M. Berggren, Ion bipolar junction transistors. *Proc. Natl. Acad. Sci. U.S.A.* **107**, 9929–9932 (2010). doi:10.1073/pnas.0913911107 Medline

23. A. S. Shaplov, P. S. Vlasov, E. I. Lozinskaya, D. O. Ponkratov, I. A. Malyshkina, F. Vidal, O. V. Okatova, G. M. Pavlov, C. Wandrey, A. Bhide, M. Schönhoff, Y. S. Vygodskii, Polymeric Ionic Liquids: Comparison of Polycations and Polyanions. *Macromolecules* **44**, 9792–9803 (2011). doi:10.1021/ma2014518

24. H. Chen, J.-H. Choi, D. Salas-de la Cruz, K. I. Winey, Y. A. Elabd, Polymerized Ionic Liquids: The Effect of Random Copolymer Composition on Ion Conduction. *Macromolecules* **42**, 4809–4816 (2009). doi:10.1021/ma900713e

25. F. Fan, W. Wang, A. P. Holt, H. Feng, D. Uhrig, X. Lu, T. Hong, Y. Wang, N.-G. Kang, J. Mays, A. P. Sokolov, Effect of Molecular Weight on the Ion Transport Mechanism in Polymerized Ionic Liquids. *Macromolecules* **49**, 4557–4570 (2016). doi:10.1021/acs.macromol.6b00714

26. J. A. Rogers, T. Someya, Y. Huang, Materials and mechanics for stretchable electronics. *Science* **327**, 1603–1607 (2010). doi:10.1126/science.1182383 Medline

27. J.-H. Choi, W. Xie, Y. Gu, C. D. Frisbie, T. P. Lodge, Single ion conducting, polymerized ionic liquid triblock copolymer films: High capacitance electrolyte gates for n-type transistors. *ACS Appl. Mater. Interfaces* **7**, 7294–7302 (2015). doi:10.1021/acsami.5b00495 Medline

28. Y. Wang, Z. Wang, Z. Su, S. Cai, Stretchable and transparent ionic diode and logic gates. *Extreme Mech. Lett.* **28**, 81–86 (2019). doi:10.1016/j.eml.2019.03.001

29. M. Lallart, P.-J. Cottinet, D. Guyomar, L. Lebrun, Electrostrictive polymers for mechanical energy harvesting. *J. Polym. Sci. B* **50**, 523–535 (2012). doi:10.1002/polb.23045

30. S. H. Kim, C. S. Haines, N. Li, K. J. Kim, T. J. Mun, C. Choi, J. Di, Y. J. Oh, J. P. Oviedo, J. Bykova, S. Fang, N. Jiang, Z. Liu, R. Wang, P. Kumar, R. Qiao, S. Priya, K. Cho, M. Kim, M. S. Lucas, L. F. Drummy, B. Maruyama, D. Y. Lee, X. Lepró, E. Gao, D. Albarq, R. Ovalle-Robles, S. J. Kim, R. H. Baughman, Harvesting electrical energy from carbon nanotube yarn twist. *Science* **357**, 773–778 (2017). doi:10.1126/science.aam8771 Medline

31. H. Kim, B. Chen, Z. Suo, R. C. Hayward, Ionoelastomer Junctions Between Polymer Networks of Fixed Anions and Cations, 104, Data and Datasets, ScholarWorks at UMass Amherst (2019); https://doi.org/10.7275/k23d-6081.

32. D. J. Lipomi, M. Vosgueritchian, B. C.-K. Tee, S. L. Hellstrom, J. A. Lee, C. H. Fox, Z. Bao, Skin-like pressure and strain sensors based on transparent elastic films of carbon nanotubes. *Nat. Nanotechnol.* **6**, 788–792 (2011). doi:10.1038/nnano.2011.184 Medline

33. Y. Gao, K. Wu, Z. Suo, Photodetachable adhesion. *Adv. Mater.* **31**, e1806948 (2019). doi:10.1002/adma.201806948 Medline

34. G. J. Brug, A. L. G. van den Eeden, M. Sluyters-Rehbach, J. H. Sluyters, The analysis of electrode impedances complicated by the presence of a constant phase element. *J. Electroanal. Chem.* **176**, 275–295 (1984). doi:10.1016/S0022-0728(84)80324-1

35. M. E. Orazem, I. Frateur, B. Tribollet, V. Vivier, S. Marcelin, N. Pébère, A. L. Bunge, E. A. White, D. P. Riemer, M. Musiani, Dielectric Properties of Materials Showing Constant-Phase-Element (CPE) Impedance Response. *J. Electrochem. Soc.* **160**, C215–C225 (2013). doi:10.1149/2.033306jes

36. V. F. Lvovich, *Impedance Spectroscopy: Applications to Electrochemical and Dielectric Phenomena* (Wiley, 2012).

37. M. A. Gebbie, A. M. Smith, H. A. Dobbs, A. A. Lee, G. G. Warr, X. Banquy, M. Valtiner, M. W. Rutland, J. N. Israelachvili, S. Perkin, R. Atkin, Long range electrostatic forces in ionic liquids. *Chem. Commun.* **53**, 1214–1224 (2017). doi:10.1039/C6CC08820A Medline

38. H. Tokuda, S. Tsuzuki, M. A. B. H. Susan, K. Hayamizu, M. Watanabe, How ionic are room-temperature ionic liquids? An indicator of the physicochemical properties. *J. Phys. Chem. B* **110**, 19593–19600 (2006). doi:10.1021/jp064159v Medline

39. U. H. Choi, M. Lee, S. Wang, W. Liu, K. I. Winey, H. W. Gibson, R. H. Colby, Ionic Conduction and Dielectric Response of Poly(imidazolium acrylate) Ionomers. *Macromolecules* **45**, 3974–3985 (2012). doi:10.1021/ma202784e